Visualizing core-shell structure of heavily doped silicon quantum dots by electron microscope using atomically thin support film

Journal:	*Nanoscale*
Manuscript ID	NR-COM-12-2017-009474.R1
Article Type:	Communication
Date Submitted by the Author:	01-Mar-2018
Complete List of Authors:	Sugimoto, Hiroshi; Kobe University, Department of Electrical and Electronic Engineering Yamamura, Masataka; Kobe University, Department of Electrical and Electronic Engineering Sakiyama, Makoto; Kobe University, Department of Electrical and Electronic Engineering Fujii, Minoru; Kobe University, Department of Electrical and Electronic Engineering, Graduate School of Engineering

Journal Name

COMMUNICATION

Visualizing core-shell structure of heavily doped silicon quantum dots by electron microscope using atomically thin support film

Received 00th January 20xx,
Accepted 00th January 20xx

DOI: 10.1039/x0xx00000x

www.rsc.org/

H. Sugimoto[a†], M. Yamamura[a], M. Sakiyama[a], M. Fujii[a]

We successfully visualize a core-shell structure of a heavily B and P codoped Si quantum dot (QD) by transmission electron microscope using an ultra-thin graphene oxide support film. The enhanced contrast reveals that a codoped Si QD has a highly crystalline Si core and an amorphous shell composed of Si, B and P.

Colloidal semiconductor quantum dots (QDs) are considered to be a key material in realizing solution-processed optoelectronic devices and are also attracting attentions as efficient and stable phosphors in bio-imaging and sensing.[1–3] The most important feature of a colloidal QD is the size-tunable electronic and optical properties arising from the quantum size effect. To fully exploit the benefit of the quantum size effect, it is important to properly design and engineer the surface structure. In Cd chalcogenide and Pb chalcogenide QDs, epitaxial growth of a wider band gap shell on a narrower band gap QD core leads to effective carrier confinement.[4–6] The core-shell structure extends the freedom of design of the energy state structure and significantly improves the luminescence quantum efficiency and the stability.[7–10]

A concern in Cd and Pb chalcogenide QDs is the toxicity of the heavy metals, which limits the applications in fundamental researches. A promising alternative to the heavy-metal-based QDs is a Si QD, which has been attracting attentions as an environmentally benign nanomaterial towards optoelectronic devices[11–14] and biomedical applications.[15,16] Thanks to the recent development of the growth technology,[17–22] the quality of colloidal Si QDs such as the colloidal stability and the luminescence quantum efficiency has been rapidly catching up.

One of the remaining problems of Si QDs is the lack of a standard process to produce a core-shell structure. Since there is no lattice-matched wide band gap semiconductor for Si crystal, it is not straightforward to produce a core-shell structure similar to Cd and Pb chalcogenide QDs. As a result, in almost all cases, organic ligands are directly attached on the surface of a Si QD core and play a role of a wide band gap shell.[23–25] Formation of covalent Si-C bonds on the surface by hydrosilylation effectively passivates surface defects.[23–28] Furthermore, long alkyl chains provide the colloidal stability by the steric barriers. However, organic-functionalized Si QDs are often not very stable in air and in other harsh environment. Sometimes, the luminescence property is determined by the surface defect states rather than the quantum size effect.[23] Amorphous SiO_2 is also a material of a wide band gap shell for a Si QD. Lin et al., developed water dispersible Si QDs with oxide shells.[29] However, the observed luminescence was blue,[23,29] which is usually considered to arise from defect states[30].

As a new class of core-shell colloidal Si QDs, we have recently developed a boron (B) and phosphorus (P) codoped Si QD.[19,31–35] Codoped Si QDs have negative surface potential (zeta potential: ~−30 mV at pH 7) and they are dispersible in water and alcohol without organic ligands.[19,32] The codoped Si QDs exhibit size-tunable photoluminescence (PL) in a wide energy range in solution and in air.[32,36,37] Atom probe tomography (APT)[38] and X-ray photoelectron spectroscopy (XPS)[31,39] analyses revealed that doped B and P are accumulated on or near the surface of Si QDs and form a high B and P concentration (> 1 at.%) shell. Preferential accumulation of B and P near a Si QD surface is predicted by ab-initio calculations.[40–43] However, the direct observation of the shell by transmission electron microscope (TEM) has not been successful and the structure has not been clarified.

Recently, Panthani et al., succeeded in imaging organic ligands on Si QDs[44] by high-resolution (HR) TEM using a graphene support film.[45] Graphene is smooth and atomically thin, and provides enhanced contrast, which makes observation of amorphous structure on the surface of Si QDs possible. In this work, we visualize the shell of codoped Si QDs by a similar method. We use graphene oxide instead of graphene for a better affinity with hydrophilic codoped Si QDs. We show that the shell is amorphous and the thickness

---

[a] *Department of Electrical and Electronic Engineering, Graduate School of Engineering, Kobe University, Rokkodai, Nada, Kobe 657-8501, Japan.*
† Corresponding Author e-mail : sugimoto@eedept.kobe-u.ac.jp

depends on the doping concentration. We also discuss the composition of the amorphous shell from XPS and Raman spectroscopy data.

Codoped colloidal Si QDs were prepared by a cosputtering method.[32,46] Briefly, Si-rich borophosphosilicate glass (BPSG) films were first deposited on a stainless steel plate by simultaneously sputtering Si, SiO_2, B_2O_3 and P_2O_5. Films of two different B and P concentrations were prepared as summarized in Table 1. Hereafter, we refer the samples by the name given in Table 1. The films were then peeled off from the plate and annealed in a N_2 gas atmosphere at 1200°C for 30 min to grow Si QDs. During the growth of Si QDs, parts of B and P atoms are reduced by excess Si and form a high B and P concentration shell.[47] Si QDs grown in BPSG matrices were liberated from matrices by hydrofluoric acid (HF) etching, and then dispersed in methanol.

Table 1. List of samples. B and P concentrations are those in sputter-deposited Si-rich BPSG films before annealing.

Sample	B concentration (at.%)	P concentration (at.%)
HT1200	0.86	0.62
LT1200	0.80	0.29

Figure 1(a) and (b) show the photos and TEM images of HT1200 and LT1200, respectively. In both samples, clear colloidal dispersions of QDs are obtained and isolated QDs can be seen in the TEM images. The size-distributions estimated from the TEM images are shown in Figure 1(c). The average diameter (D_{ave}) of HT1200 is 7.0 nm with the standard deviation (σ) of 1.4 nm, while D_{ave} of LT1200 is 6.8 nm with σ of 1.1 nm.

Figure 1(d) shows infrared (IR) absorption spectra of codoped Si QDs just after preparation (stored in methanol within an hour). Peaks at 850-900 and ~2100 cm^{-1} are assigned to Si-H_x scissors and stretching vibration modes,[48,49] respectively, and that at 1080 cm^{-1} is assigned to Si-O-Si stretching modes. Considering the approximately 20 times larger oscillator strength of the Si-O-Si stretching mode than that of the Si-H stretching mode,[50,51] we can estimate that 99% of the surface of codoped QDs is terminated by H and 1% by O in both samples. It should be stressed here that H-terminated Si is usually strongly hydrophobic. Concomitance of H-termination and hydrophilicity has been a kind of mystery in codoped Si QDs. In this work, we focus on H-terminated Si QDs; all the experimental data are taken within an hour after the HF etching unless otherwise designated to prevent surface oxidation.

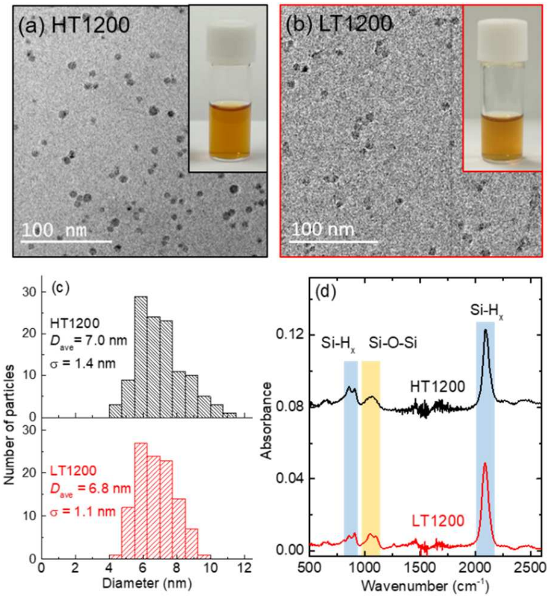

Figure 1. (a, b) Photos of methanol solutions of B and P codoped Si QDs and the TEM images, (a) HT1200 and (b) LT1200. (c) Size distributions and (d) IR absorption spectra of HT1200 and LT1200.

Figure 2(a) shows a typical HRTEM image of a B and P codoped Si QD (HT1200) on a conventional TEM grid with an amorphous carbon support film (10 nm in thickness). The HRTEM observations are performed with JEOL JEM-2100F operated at 200keV. We can see Si QD 5.5 nm in diameter with the lattice fringe corresponds to {111} planes of diamond structure crystalline Si (lattice spacing: 0.31 nm). Figure 2(b) shows the

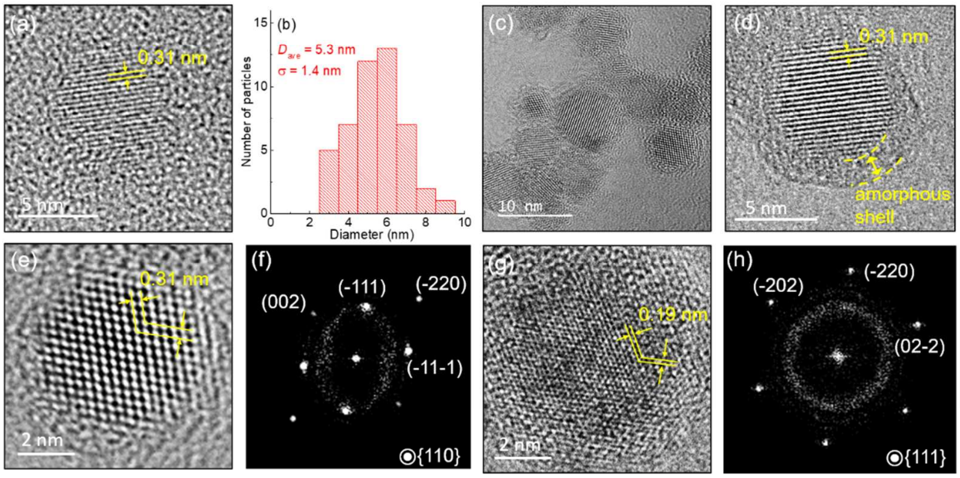

Figure 2 (a) HRTEM image of codoped Si QDs (HT1200) on an amorphous carbon film. (b) Size-distribution of crystalline Si cores obtained from HRTEM images. (c, d) HRTEM images of codoped Si QDs (HT1200) on graphene oxide support films. (e, f) HRTEM image of a codoped QD with the corresponding FFT image. (g, h) HRTEM image of a codoped QD with the corresponding FFT image.

size distribution obtained from Si QDs with clear lattice fringes in HRTEM images. The average diameter is 5.3 nm, which is 1.7 nm smaller than that obtained from lower magnification images shown in Figure 1(c). The difference may suggest the existence of a shell, which is not observed as lattice fringes in HRTEM images.

In order to visualize the shell, we use an atomically thin graphene oxide support film, which is prepared by drop-casting a methanol solution of graphene oxide produced by the Hummer's method[52] onto lacey carbon-coated copper TEM grids (Oken Shoji Co.). Figure 2(c) shows a HRTEM image of HT1200 on a graphene oxide support film. In Figure 2(d), an enlarged image of a QD is shown. Thanks to the significant decrease of the background noise from an amorphous carbon support film, an amorphous shell can clearly be visualized. It should be stressed here that the shell is not SiO_x, since the surface of codoped Si QDs within an hour after preparation (*i.e.*, after HF etching) is 99% H-terminated as shown in the IR absorption spectra in Figure 1(d). We will discuss the constituents of the shell later.

The reduction of the background noise also enables detailed analyses of the crystalline structure. Figure 2(e) and (g) shows the representative HRTEM images of codoped Si QDs (HT1200), and Figure 2(f) and (h) are corresponding fast Fourier transform (FFT) images, respectively. Cross-fringes with different lattice spacing are clearly seen in the TEM images. All spots in Figure 2(f) and (h) are assigned to different planes with {110} and {111} zone axes, respectively. The lattice spacing of {111} and {220} planes are 0.31 and 0.19 nm, which coincide very well with those of the diamond structure crystalline Si.

Figure 3(a)-(c) shows the HRTEM images of different size QDs in the size distribution in HT1200. The diameters are (a) 9.0, (b) 5.2 and (c) 4.0 nm. In all these QDs, we can see a crystalline Si core and an amorphous shell. In Figure 3(g), we plotted the shell thickness as a function of the core diameter (HT1200: black circle). The shell thickness is distributed from 0.85 to 1.4 nm and is independent of the core diameter. In order to exclude the possibility that the shell is hydrocarbon contamination accumulated during the HF etching process, for some samples, we performed ion cleaning (EC-52000IC, JEOL) prior to the HRTEM observation. The representative HRTEM images of QDs (HT1200) after the cleaning are shown in Supporting Information (Figure S1). No changes were observed in the structure of Si QDs. In Figure 3(h), the shell thicknesses obtained from HRTEM images of ion-cleaned HT1200 are plotted. The thickness is in the same range as those in Fig. 3 (g).

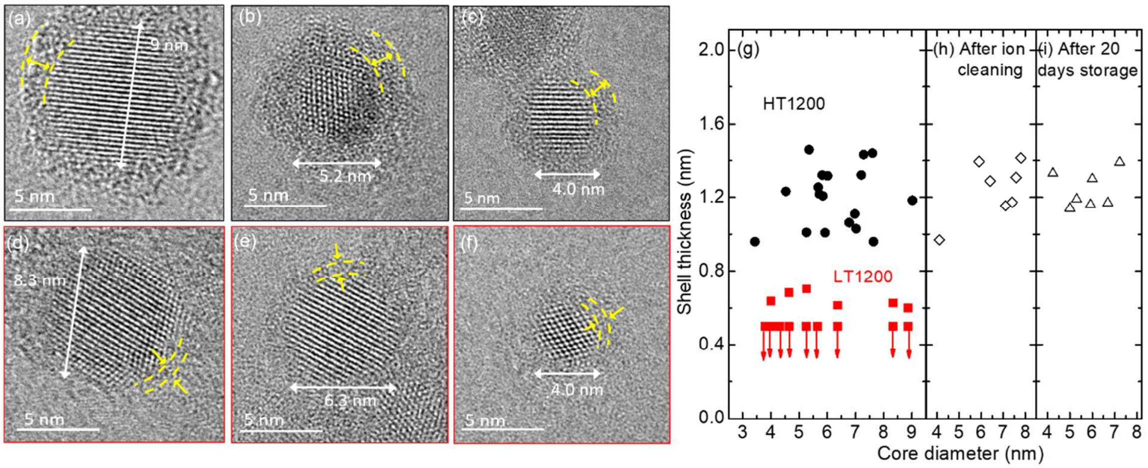

Figure 3. HRTEM images of codoped QDs in (a-c) HT1200 and (d-f) LT1200. (g) Shell thicknesses of HT1200 and LT1200 as a function of core diameter. Down arrows indicate that the thickness is below 0.5 nm. Shell thicknesses of HT1200 (h) after ion cleaning and (i) after 20 days storage in methanol.

In order to study the relation between the doping concentration and the shell thickness, we perform TEM observations of a lower doping concentration sample (LT1200). Figure 3(d)-(f) show the results. We select QDs with the diameters similar to those in Figure 3(a)-(c) in the size distribution. The crystalline Si core can clearly be seen. On the other hand, the amorphous shell is much thinner than that in HT1200 and in many cases hard to be observed. This can be seen in Figure 3(g) (red square). The down arrows mean that the thickness is below 0.5 nm and cannot be measured accurately. The shell thickness is below 0.7 nm in LT1200 and there is no size dependence. The clear difference of the shell thickness between HT1200 and LT1200 indicates that doping concentration is the decisive factor to determine the thickness.

For the investigation of the composition and chemical states of the amorphous shell, XPS is a powerful tool due to the small escape depth of photoelectrons (2.0-2.7 nm).[53] For XPS measurements, a solution of codoped Si QDs was deposited on a gold-coated stainless steel plates. Note again that the measurements were performed within an hour after preparation to prevent surface oxidation. Figure 4(a)-(c) shows Al Kα XPS spectra of codoped Si QDs (HT1200 and LT1200) (PHI X-tool, ULVAC-PHI). In the Si 2p signals (Figure 4(a)), a major peak at 99.6 eV is assigned to neutral Si (Si^0), while a small shoulder at the higher energy side is assigned to oxidized states of Si, *i.e.*, Si^{1+}, Si^{2+}, Si^{3+} and Si^{4+}. The Si^0 signal intensity of HT1200 is much smaller than that of LT1200. This indicates that the major part of the Si^0 signal arises from a Si QD core and the thicker shell in HT1200 obstructs the escape of core photoelectrons from a QD.

In P 2p spectra in Figure 4(b), the peak is around 130 eV, which can be assigned to neutral P. Majority of P atoms are thus non-oxidized states. As is expected from the preparation parameters in Table 1, the signal intensity is larger in HT1200 than in LT1200. Therefore, P concentration in codoped Si QDs is controlled by the preparation parameters.

B 1s signal around 187-188 eV in Figure 4(c) can be assigned to neutral B, and thus majority of B atoms exist also as the non-oxidized states. The signal intensity is again much larger in HT1200 than in LT1200. However, this is not consistent with the preparation parameters shown in Table 1, where the B concentration is almost the same in the two samples. The larger B concentration in HT1200 than that expected from the B concentration in the Si-rich BPSG film suggests that P plays a role of an anchor to incorporate more B in or on the surface of Si QDs.

From the XPS data, we can estimate the atomic composition (Si: B: P) by taking into account the ionization cross-sections of each element. In HT1200, the atomic ratio of Si, B and P is 78.8: 13.1: 8.1, while in LT1200, it is 92.9: 4.4: 2.7. The B and P concentrations are much larger than their solid solubilities in Si crystal (~1 %).[54] Therefore, majority of B and P are considered to exist in the amorphous shell. Under the assumption that the Si^0 signal arises solely from crystalline Si cores, the composition of the amorphous shell (Si: B: P) is estimated by subtracting the signal of Si^0 from the spectra. The obtained compositions (Si: B: P) are 55.0: 27.7: 17.3 in HT1200 and 72.3: 17.0 10.7 in LT1200. The shell is thus an amorphous material composed of Si, B and P.

The IR absorption and XPS data suggest that the surface of the amorphous shell is mainly terminated by H and partly by O. Furthermore, surface O atoms have bonds mainly with Si and those with B and P are very rare. In the Si 2p spectra in Figure 4(a), in LT1200, the intensities of the different oxidation states (Si^{1+} to Si^{4+}) are similar. On the other hand, in HT1200, the Si^{4+} signal is much weaker than those of other oxidation states. The smaller Si^{4+} signal in HT1200 suggests that the high B concentration in the shell prevents the surface to proceed to the higher oxidation state.

In order to obtain information on the structure of the shell, we measure the Raman spectra. For the Raman measurements, a solution of codoped Si QDs was deposited on a gold-coated Si wafer and a micro-Raman setup was used (50x objective lens, NA=0.8). The excitation wavelength was 514.5 nm and the power was 1 mW. Figure 4(d) compares the Raman spectra of HT1200 and LT1200. As a reference, the spectrum of undoped Si QDs is also shown. A major peak at 515-520 cm^{-1} is assigned to transverse optical (TO) phonons in crystalline Si.

A characteristic feature in the Raman spectra of codoped Si QDs is a broad band at 600-700 cm^{-1}, which does not exist in undoped Si QDs. There are several possible origins of the band. One is the local vibration modes of B^{10} and B^{11} in crystal Si at 620 and 640 cm^{-1}, respectively. However, they cannot fully explain the observed band because of the two reasons. The first one is the intensity. The relative intensity of the signal to the main peak of Si crystal is too large for the local mode, even if the B concentration is close to the solid solubility limit.[55] The other one is that the band has a large intensity above the wavenumbers of B^{11} (620 cm^{-1}) and B^{10} (640 cm^{-1}) local modes. Another possible origin of the band is Si-B stretching vibration modes in Si_mB_n (m=1-8, n=1-4, 6) clusters. Depending on the compositions, the clusters have vibration modes in the range of 650-700 cm^{-1}.[56–58] Therefore, it is very plausible that the higher wavenumber side of the 600-700 cm^{-1} band arises from Si_mB_n clusters, and they are the constituents of the amorphous shell. This model can explain the different spectral shape between HT1200 and LT1200. Growth of a thicker shell in HT1200 results in larger Raman intensity at the higher wavenumber side of the band.

As we estimated from XPS spectra, the P concentration in the shell is comparable or even larger than the B concentration. Therefore, it is very plausible that the clusters constituting the shell also contain P, and $Si_mB_nP_l$ clusters are formed. The lower wavenumber side of the peak of crystal Si (~520 cm^{-1}) in Raman spectra may suggest the existence of the $Si_mB_nP_l$ clusters. Despite very high crystallinity of the Si QD cores proved by HRTEM observations, the Raman signal in the region is stronger in codoped Si QDs than in undoped Si QDs. This suggests that the low wavenumber tail cannot be fully explained by the distortion of the crystalline Si core, but may arise from the amorphous shell. In fact, there is a positive correlation between the intensity of the low wavenumber tail and the 650-700 cm^{-1} band. It is known that B_nP_l clusters have P-P vibration Raman modes around 480 cm^{-1}.[59] Therefore, our tentative assignment of the signal in the lower wavenumber region is that they are due to P-P vibration modes in $Si_mB_nP_l$ clusters in the shell.

Up to now, we study the structure of codoped Si QDs just after preparation, *i.e.*, within one hour after the HF etching. We also study the effect of oxidation on the structure. When we store HT1200 in methanol for 20 days, the replacement of surface H atoms with O atoms proceeds and the number ratio of Si-H to Si-O decreases from 99% to 51% (Supporting Information, Figure S2(a)). However, it does not affect the Raman spectral shape at all (Supporting Information, Figure S2(b)). Therefore, the replacement of surface H atoms with O atoms does not affect the structure of the shell. In Figure 3(i), the shell thickness distribution obtained from HRTEM images of HT1200 after 20 days storage in methanol is shown. The shell thickness is in the same range as that of HT1200 just after preparation.

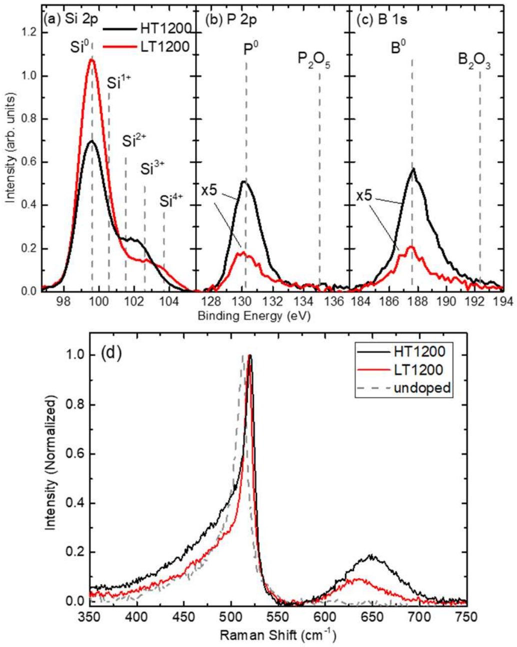

Figure 4. XPS spectra of HT1200 and LT1200. (a) Si 2p, (b) P 2p, and (c) B 1s. (d) Raman scattering spectra of undoped Si QDs (dashed grey), HT1200 (black) and LT1200 (red).

Conclusions

We have performed TEM observations of heavily B and P codoped Si QDs using an atomically-flat graphene oxide support film. We found that a codoped Si QD consists of a highly crystalline Si core and an amorphous shell. The shell thickness depends on the B and P concentrations in starting materials. XPS and Raman analyses reveal that the amorphous shell is composed of various type of clusters composed of Si, B and P. This amorphous shell is responsible for the characteristic features of codoped Si QDs, especially the concomitance of the high solubility in polar solvents and H-termination.

Acknowledgements

This work was partly supported by the 2015 JST Visegrad Group (V4)–Japan Joint Research Project on Advanced Materials and JSPS KAKENHI Grant Number 16H03828.

Notes and references

1 H. Sargent and E. H. Sargent, *Nat. Photonics*, 2012, **6**, 133–135.
2 Y. Shirasaki, G. J. Supran, M. G. Bawendi and V. Bulović, *Nat. Photonics*, 2012, **7**, 13–23.
3 J. Yao, M. Yang and Y. Duan, *Chem. Rev.*, 2014, **114**, 6130–6178.
4 S. Kim, B. Fisher, H.-J. Eisler and M. Bawendi, *J. Am. Chem. Soc.*, 2003, **125**, 11466–11467.
5 B. O. Dabbousi, J. Rodriguez-Viejo, F. V Mikulec, J. R. Heine, H. Mattoussi, R. Ober, K. F. Jensen and M. G. Bawendi, *J. Phys. Chem. B*, 1997, **101**, 9463–9475.
6 P. Reiss, J. Bleuse and A. Pron, *Nano Lett.*, 2002, **2**, 781–784.
7 O. Chen, J. Zhao, V. P. Chauhan, J. Cui, C. Wong, D. K. Harris, H. Wei, H.-S. Han, D. Fukumura, R. K. Jain and M. G. Bawendi, *Nat. Mater.*, 2013, **12**, 445–451.
8 S. Kim, B. Fisher, H.-J. Eisler and M. Bawendi, *J. Am. Chem. Soc.*, 2003, **125**, 11466–11467.
9 B. O. Dabbousi, J. Rodriguez-Viejo, F. V Mikulec, J. R. Heine, H. Mattoussi, R. Ober, K. F. Jensen and M. G. Bawendi, *J. Phys. Chem. B*, 1997, **101**, 9463–9475.
10 P. Reiss, J. Bleuse and A. Pron, *Nano Lett.*, 2002, **2**, 781–784.
11 F. Maier-Flaig, J. Rinck, M. Stephan, T. Bocksrocker, M. Bruns, C. Kübel, A. K. Powell, G. A. Ozin and U. Lemmer, *Nano Lett.*, 2013, **13**, 475–480.
12 K.-Y. Cheng, R. Anthony, U. R. Kortshagen and R. J. Holmes, *Nano Lett.*, 2011, **11**, 1952–1956.
13 Z. Ni, L. Ma, S. Du, Y. Xu, M. Yuan, H. Fang, Z. Wang, M. Xu, D. Li, J. Yang, W. Hu, X. Pi and D. Yang, *ACS Nano*, 2017, **11**, 9854–9862.
14 S. Zhao, X. Liu, W. Gu, X. Liang, Z. Ni, H. Tan, K. Huang, Y. Yan, X. Yu, M. Xu, X. Pi and D. Yang, *IEEE Trans. Electron Devices*, 2018, **65**, 577–583.
15 F. Erogbogbo, C.-A. Tien, C.-W. Chang, K.-T. Yong, W.-C. Law, H. Ding, I. Roy, M. T. Swihart and P. N. Prasad, *ACS Nano*, 2011, **2**, 873–878.
16 L. Ostrovska, A. Broz, A. Fucikova, T. Belinova, H. Sugimoto, T. Kanno, M. Fujii, J. Valenta and M. H. Kalbacova, *RSC Adv.*, 2016, **6**, 63403–63413.
17 C. M. Hessel, D. Reid, M. G. Panthani, M. R. Rasch, B. W. Goodfellow, J. Wei, H. Fujii, V. Akhavan and B. A. Korgel, *Chem. Mater.*, 2012, **24**, 393–401.
18 M. Aghajamali, M. Iqbal, T. K. Purkait, L. Hadidi, R. Sinelnikov and J. G. C. Veinot, *Chem. Mater.*, 2016, **28**, 3877–3886.
19 H. Sugimoto, M. Fujii, K. Imakita, S. Hayashi and K. Akamatsu, *J. Phys. Chem. C*, 2012, **116**, 17969–17674.
20 U. R. Kortshagen, R. M. Sankaran, R. N. Pereira, S. L. Girshick, J. J. Wu and E. S. Aydil, *Chem. Rev.*, 2016, **116**, 11061–11127.
21 Y. Yu, G. Fan, A. Fermi, R. Mazzaro, V. Morandi, P. Ceroni, D.-M. Smilgies and B. A. Korgel, *J. Phys. Chem. C*, 2017, **121**, 23240–23248.
22 D. P. Puzzo, E. J. Henderson, M. G. Helander, Z. Wang, G. A. Ozin and Z. Lu, *Nano Lett.*, 2011, **11**, 1585–1590.
23 M. Dasog, G. B. De los Reyes, L. V Titova, F. A. Hegmann and J. G. C. Veinot, *ACS Nano*, 2014, **8**, 9636–9648.
24 C. M. Hessel, J. Wei, D. Reid, H. Fujii, M. C. Downer and B. A. Korgel, *J. Phys. Chem. Lett.*, 2012, **3**, 1089–1093.
25 X. Liu, Y. Zhang, T. Yu, X. Qiao, R. Gresback, X. Pi and D. Yang, *Part. Part. Syst. Charact.*, 2016, **33**, 44–52.
26 A. Angı, R. Sinelnikov, A. Meldrum, J. G. C. Veinot, I. Balberg, D. Azulay, O. Millo and B. Rieger, 2016, **8**, 7849–7853.
27 M. H. Mobarok, T. K. Purkait, M. A. Islam, M. Miskolzie and J. G. C. Veinot, *Angew. Chemie Int. Ed.*, 2017, **56**, 6073–6077.
28 M. A. Islam, M. H. Mobarok, R. Sinelnikov, T. K. Purkait and J. G. C. Veinot, *Langmuir*, 2017, **33**, 8766–8773.
29 S.-W. Lin and D.-H. Chen, *Small*, 2009, **5**, 72–76.

30 M. Dasog, Z. Yang, S. Regli, T. M. Atkins, A. Faramus, M. P. Singh, E. Muthuswamy, S. M. Kauzlarich, R. D. Tilley and J. G. C. Veinot, *ACS Nano*, 2013, **7**, 2676–2685.

31 H. Sugimoto, M. Fujii, K. Imakita, S. Hayashi and K. Akamatsu, *J. Phys. Chem. C*, 2013, **117**, 6807–6813.

32 H. Sugimoto, M. Fujii, K. Imakita, S. Hayashi and K. Akamatsu, *J. Phys. Chem. C*, 2013, **117**, 11850–11857.

33 H. Sugimoto, M. Fujii, Y. Fukuda, K. Imakita and K. Akamatsu, *Nanoscale*, 2014, **6**, 122–6.

34 H. Sugimoto, M. Fujii and K. Imakita, *Nanoscale*, 2014, **6**, 12354–12359.

35 M. Fujii, H. Sugimoto and K. Imakita, *Nanotechnology*, 2016, **27**, 262001.

36 Y. Hori, S. Kano, H. Sugimoto, K. Imakita and M. Fujii, *Nano Lett.*, 2016, **16**, 2615–2620.

37 O. Ashkenazi, D. Azulay, I. Balberg, S. Kano, H. Sugimoto, M. Fujii and O. Millo, *Nanoscale*, 2017, **9**, 17884–17892.

38 K. Nomoto, H. Sugimoto, A. Breen, A. V. Ceguerra, T. Kanno, S. P. Ringer, I. P. Wurfl, G. Conibeer and M. Fujii, *J. Phys. Chem. C*, 2016, **120**, 17845–17852.

39 M. Fujii, H. Sugimoto, M. Hasegawa and K. Imakita, *J. Appl. Phys.*, 2014, **115**, 84301.

40 F. Iori, E. Degoli, R. Magri, I. Marri, G. Cantele, D. Ninno, F. Trani, O. Pulci and S. Ossicini, *Phys. Rev. B - Condens. Matter Mater. Phys.*, 2007, **76**, 1–14.

41 R. Guerra, S. Ossicini, R. Emilia and P. Morselli, *J. Am. Chem. Soc.*, 2014, **136**, 4404–4409.

42 I. Marri, E. Degoli and S. Ossicini, *Prog. Surf. Sci.*, 2017, **92**, 375–408.

43 Z. Ni, X. Pi, S. Cottenier and D. Yang, *Phys. Rev. B*, 2017, **95**, 75307.

44 M. G. Panthani, C. M. Hessel, D. Reid, G. Casillas, M. José-Yacamán and B. A. Korgel, *J. Phys. Chem. C*, 2012, **116**, 22463–22468.

45 J. C. Meyer, C. O. Girit, M. F. Crommie and A. Zettl, *Nature*, 2008, **454**, 319–322.

46 H. Sugimoto, M. Fujii, K. Imakita, S. Hayashi and K. Akamatsu, *J. Phys. Chem. C*, 2012, **116**, 17969–17974.

47 H. Sugimoto, K. Imakita and M. Fujii, *RSC Adv.*, 2015, **5**, 98248–98253.

48 J. M. Lavine, S. P. Sawan, Y. T. Shieh and A. J. Bellezza, *Appl. Phys. Lett.*, 1993, **62**, 1099–1101.

49 C. Tsai, K. -H. Li, D. S. Kinosky, R. -Z. Qian, T. -C. Hsu, J. T. Irby, S. K. Banerjee, A. F. Tasch, J. C. Campbell, B. K. Hance and J. M. White, *Appl. Phys. Lett.*, 1992, **60**, 1700–1702.

50 S. Mukhopadhyay and S. Ray, *Appl. Surf. Sci.*, 2011, **257**, 9717–9723.

51 A. A. Langford, M. L. Fleet, B. P. Nelson, W. a. Lanford and N. Maley, *Phys. Rev. B*, 1992, **45**, 13367–13377.

52 W. S. Hummers and R. E. Offeman, *J. Am. Chem. Soc.*, 1958, **80**, 1339–1339.

53 R. Flitsch and S. I. Raider, *J. Vac. Sci. Technol.*, 1975, **12**, 305–308.

54 S. M. Sze, *New York Wiley*, 1981, 868.

55 F. Cerdeira, T. A. Fjeldly and M. Cardona, *Phys. Rev. B*, 1974, **9**, 4344–4350.

56 P. Deak, A. Gali, A. Solyom, P. Ordejon, K. Kamaras and G. Battistig, *J. Phys. Condens. Matter*, 2003, **15**, 4967–4977.

57 N. X. Truong, B. K. A. Jaeger, S. Gewinner, W. Schöllkopf, A. Fielicke and O. Dopfer, *J. Phys. Chem. C*, 2017, **121**, 9560–9571.

58 F. X. Zhang, F. F. Xu, T. Mori, Q. L. Liu and T. Tanaka, *J. Solid State Chem.*, 2003, **170**, 75–81.

59 D. R. Tallant, T. L. Aselage, A. N. Campbell and D. Emin, *Phys. Rev. B*, 1989, **40**, 5649–5656.